

1 Supplementary Figures

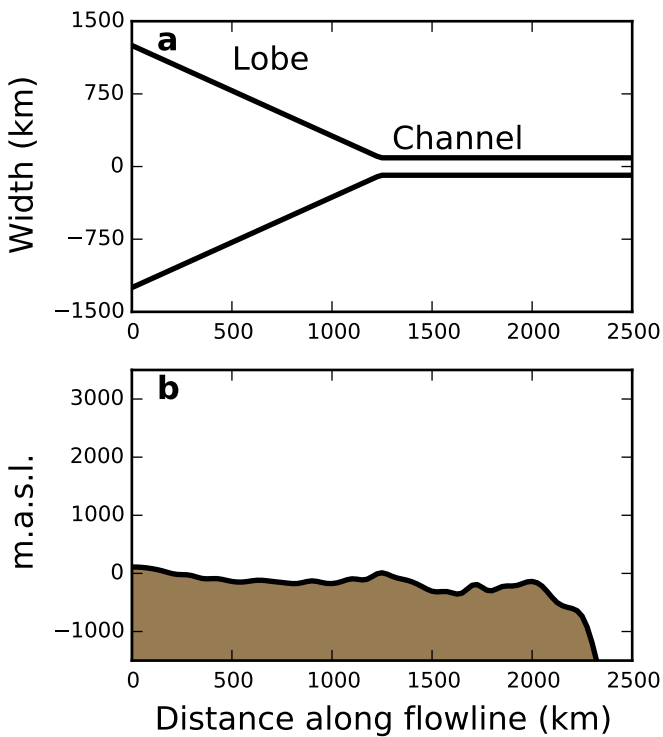


Figure S1 Geometry used in flowline and regional model simulation. Panel **a** shows
width of flowline used to approximate the geometry of the lobe of the Laurentide ice
sheet and Hudson Strait Ice Stream. The maximum width of the lobe is 2500 km and
the width of the channel is 180 km. Panel **b** shows initial, unloaded bed topography
along the flowline, obtained from ICE-5G³¹.

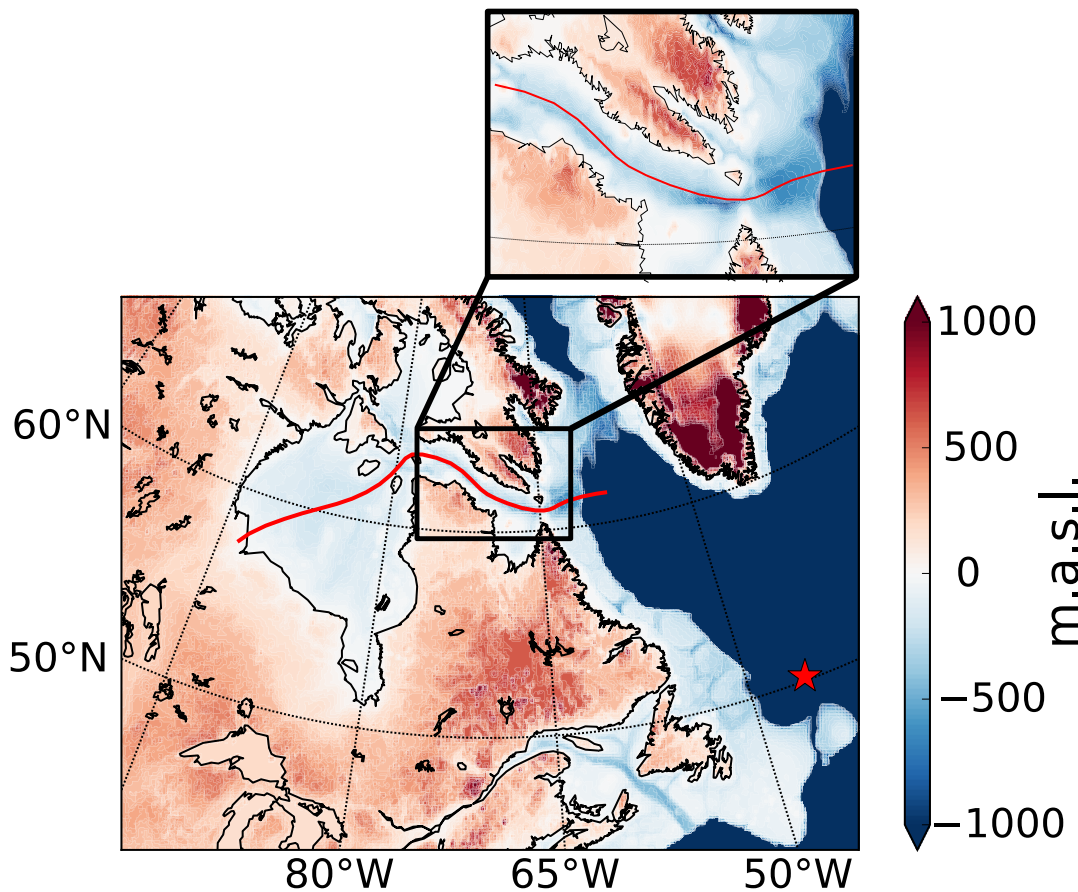


Figure S2 Map of today's bathymetry from the modern ICE-5G product³¹. The location of the selected flowline is shown in red. The red star shows the location of the sediment core MD95-2025²⁸, data from which is shown in main text Figure 2g. Inset shows a closeup of higher resolution bathymetry in the channel obtained from the ETOPO bathymetry grid, used in the regional model simulations.

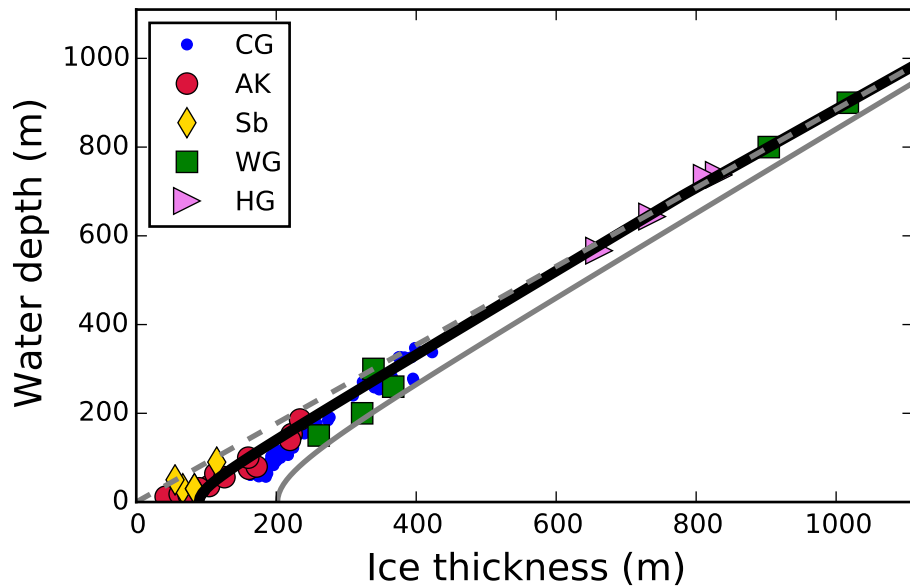
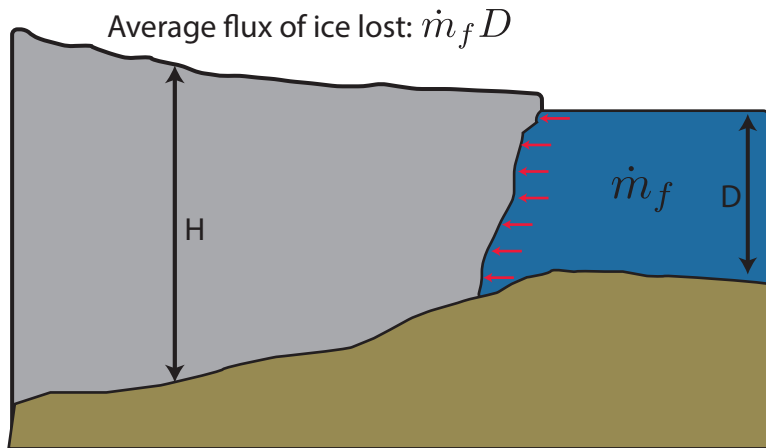
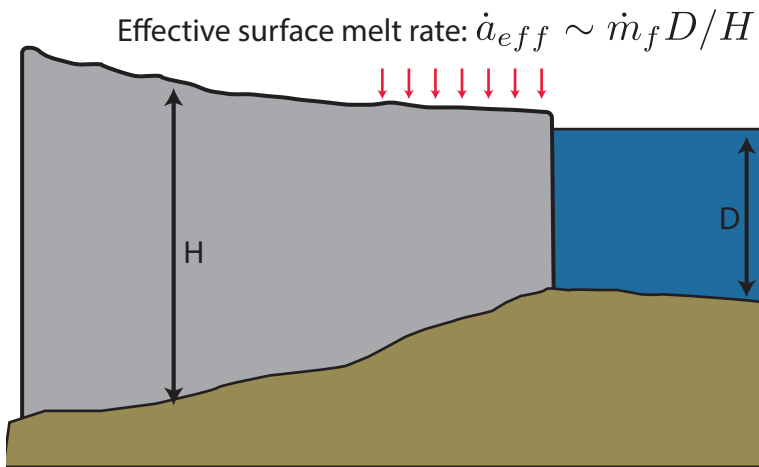


Figure S3 Fit of yield functions to observed ice thickness and water depth combinations. The solid gray line and thick black line shows ice-thickness/water depth combinations for $\tau_c = 400$ kPa and $\tau_c = 200$ kPa, respectively. The dashed gray line shows the buoyant limit. The different symbols correspond to observations of Columbia Glacier (CG), Alaska (AK), Svalbard (Sb), West Greenland (WG), Helheim Glacier (HG). All data are adapted from Bassis and Walker¹⁹.

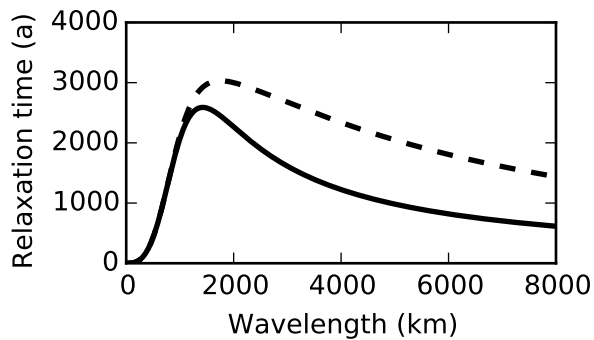
(a) Submarine melt erodes calving front



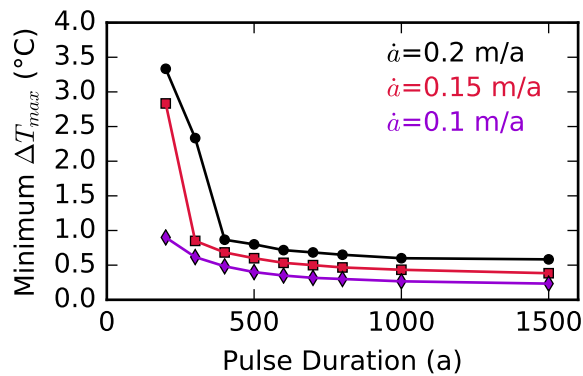
(b) Submarine melt applied as vertical surface ablation

**Figure S4** Schematic showing the implementation of submarine melt near the terminus.

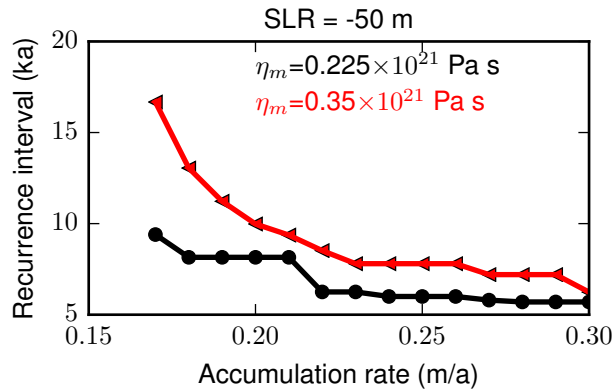
We implement submarine melt as an effective surface mass balance term that acts to thin ice near the terminus (panel b) and removes an equivalent amount of ice to that which would have been lost at the calving front (panel a).



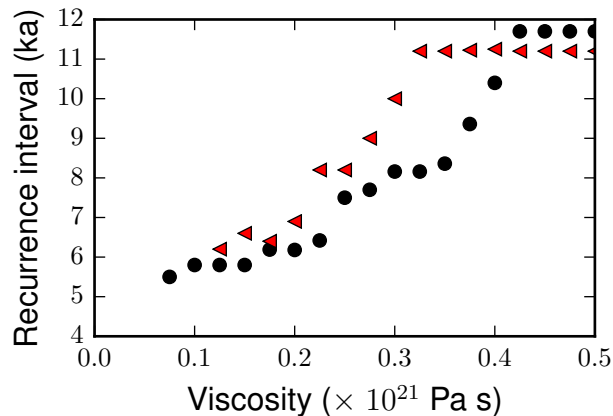
²⁷ **Figure S5** Relaxation spectrum as a function of wavelength. The solid line shows
²⁸ an elastic lithosphere with a flexural rigidity of 2.85×10^{25} N m with a uniform mantle
²⁹ viscosity of 0.4×10^{21} Pa s. Dashed line shows an upper mantle with 0.4×10^{21} Pa
³⁰ s overlying a lower mantle with viscosity 1×10^{21} Pa s. The two-layer mantle model
³¹ diverges from the one-layer model only at wavelengths greater than 1000 km. Since
³² the maximum size of our ice sheet is 2000 km, this additional layer has little impact on
³³ our results so we choose to use the one-layer model for most simulations.



35 **Figure S6** Minimum amplitude of ocean warming necessary to trigger Heinrich Events
36 for different duration of pulses and accumulation rates. All parameters are identical to
37 those shown for results in the main paper. For the majority of pulse durations and ac-
38 cumulation rates, a pulse magnitude of less than 1°C is sufficient to trigger a Heinrich
39 Event.

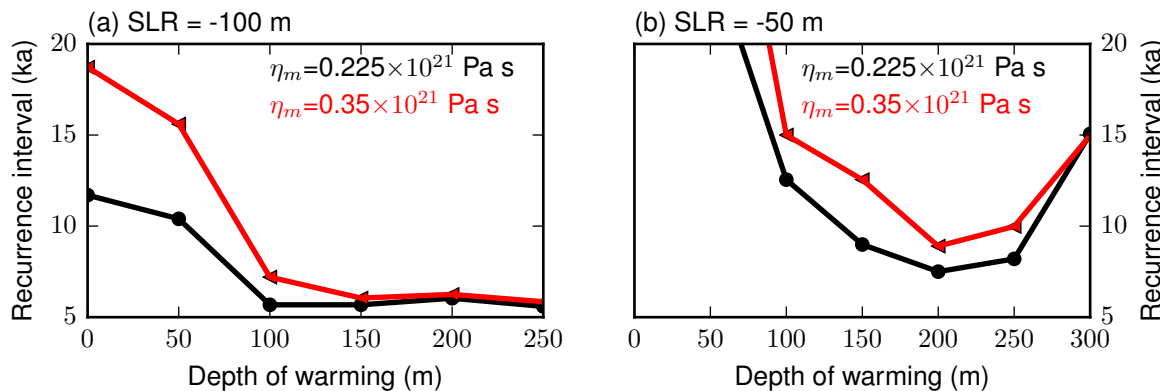


⁴¹ **Figure S7** Effect of accumulation rate on simulated recurrence intervals of Heinrich
⁴² Events. Black circles show the mean recurrence interval for an upper mantle viscosity
⁴³ of 0.225×10^{21} Pa s. Red triangles show the recurrence interval for an upper mantle
⁴⁴ viscosity of 0.35×10^{21} Pa s. All simulations were conducted with subsurface warming
⁴⁵ penetrating to a depth of 250 m and with glacial sea level (SLR) set 50 m beneath
⁴⁶ present day. The same ocean forcing was applied for all simulations. For both tested
⁴⁷ viscosities, a recurrence time of 7–10 ka, as observed in proxy records³², is produced
⁴⁸ for a large range of accumulation rates.

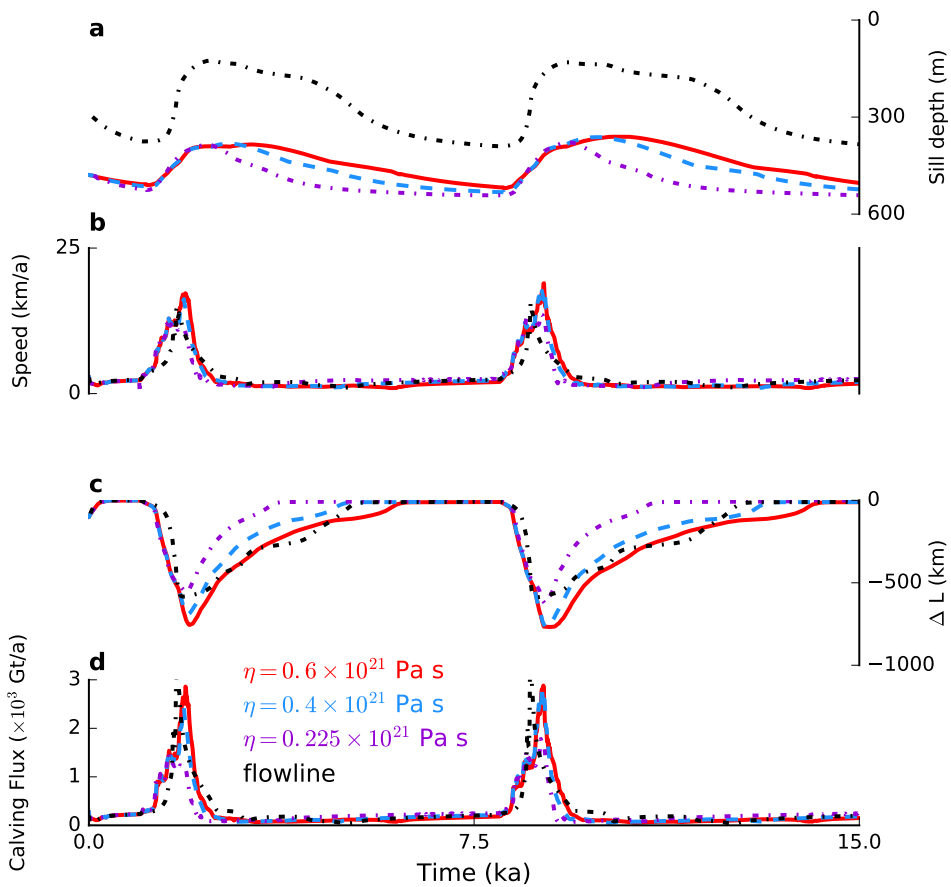


50 **Figure S8** Effect of upper mantle viscosity on recurrence interval of Heinrich Events.

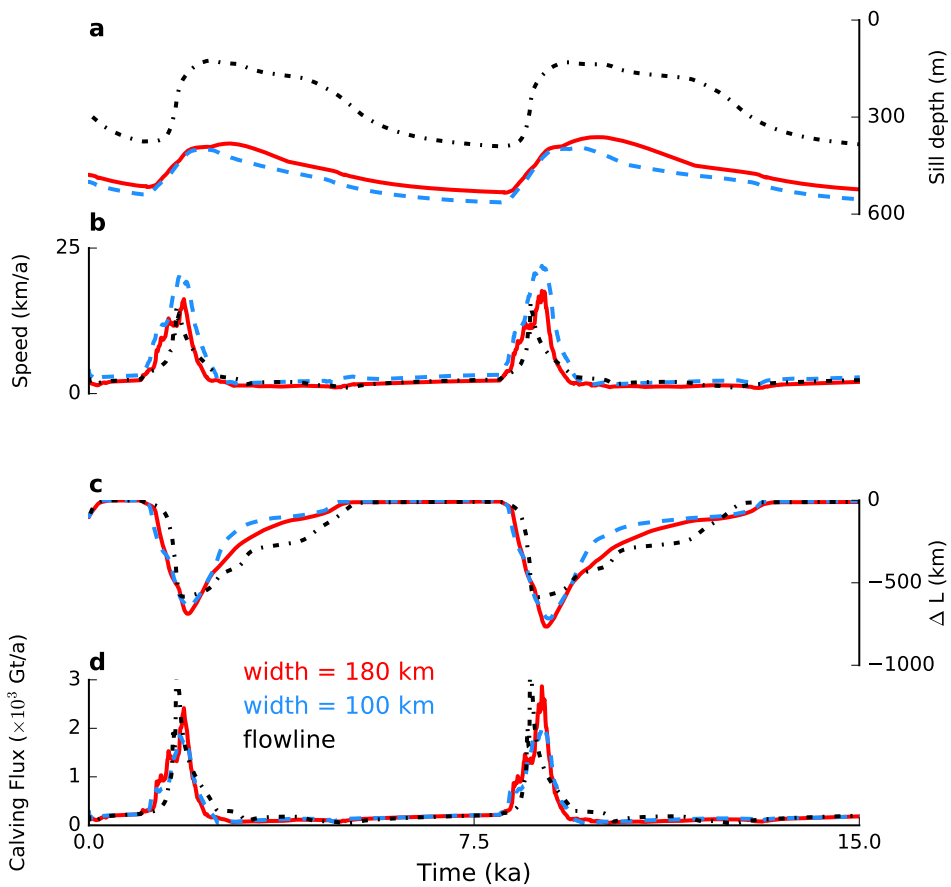
51 Black circles show the mean recurrence interval between Heinrich Events for a glacial
52 sea level 50 m below present, an accumulation rate of 0.21 m/a and a mixed layer depth
53 of 250 m. This simulation matches the timing of all Heinrich Events for a viscosity of
54 0.25×10^{21} Pa s. Red triangles show the mean recurrence interval for a glacial sea
55 level 80 m below present, an accumulation rate of 0.21 m/a and a mixed layer depth
56 of 225 m. This simulation matches the timing of all Heinrich Events for a viscosity of
57 0.35×10^{21} Pa s and of Heinrich Events H1-H6 for viscosities in the range $0.35-0.4 \times 10^{21}$
58 Pa s. The same ocean forcing function was used in all cases.



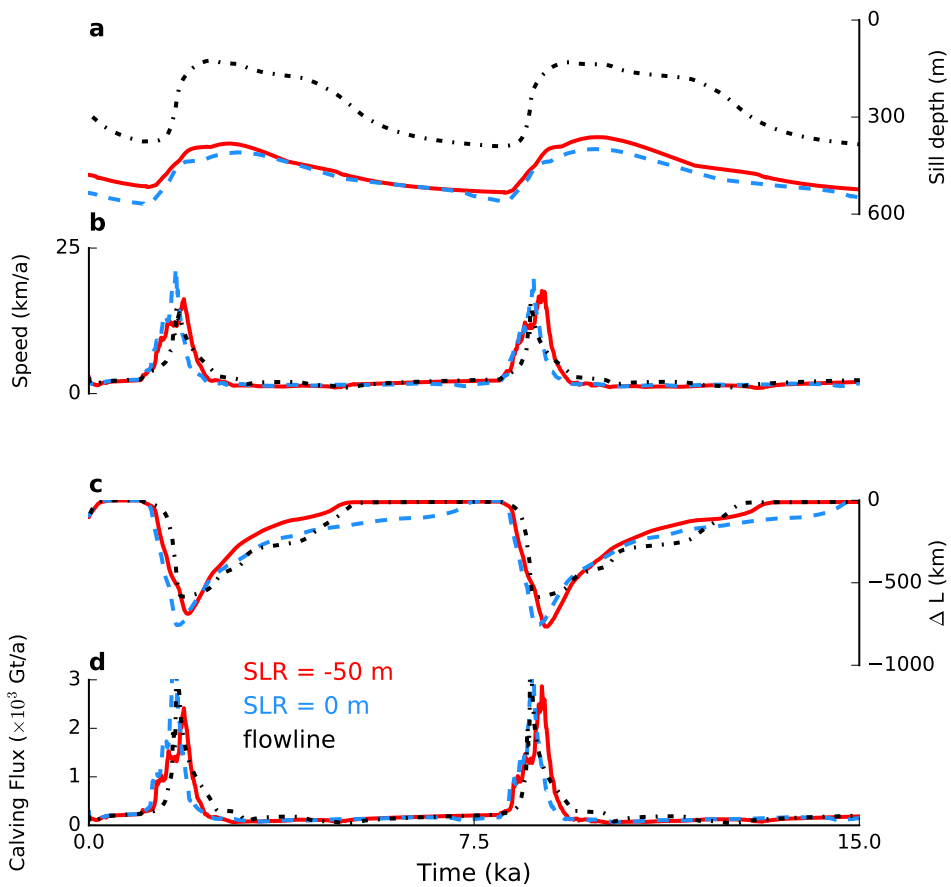
60 **Figure S9** Effect of depth of subsurface warming on simulated recurrence intervals
 61 of Heinrich Events. Panels **a** and **b** show the effect of subsurface warming for a relative
 62 sea level 100 m below present and 50 m below present for two different values of the
 63 upper mantle viscosity η_m . All simulations were conducted with an accumulation rate
 64 of 0.2 m/a.



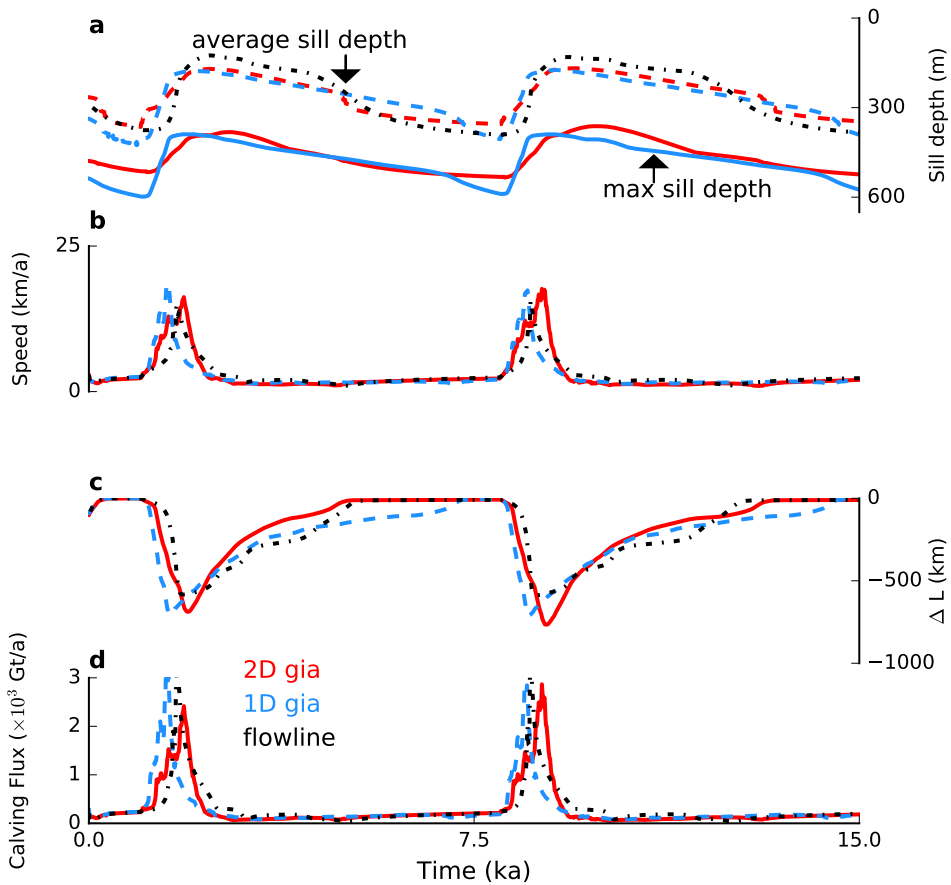
66 **Figure S10** Effect of upper mantle viscosity on Heinrich Events simulated with a re-
 67 gional model with 2D loading compared to our reference flowline model. Panel **a** shows
 68 the deepest portion of the sill for the regional model and width averaged sill for the flow-
 69 line model. Panels **b-d** show width averaged speed, change in terminus position and
 70 calving flux for the three regional model simulations. We obtain a time scale of advance
 71 from the fully retreated to the most advanced position that is most comparable to the
 72 reference flowline model when the regional model has an upper mantle viscosity of
 73 $\sim 0.4 \times 10^{21}$ Pa s. The results for all three simulations are qualitatively unchanged from
 74 the base flowline scenario. Ocean forcing corresponds to pulses at 1 ka and 8 ka.



76 **Figure S11** Effect of Hudson Strait width on simulated Heinrich Events using a re-
 77 gional model. Panel **a** shows the deepest portion of the sill for the regional model and
 78 width averaged sill for the flowline model. Panels **b-d** show width averaged speed,
 79 change in terminus position and calving flux. We obtain comparable results for widths
 80 of 100 km and 180 km, but calving fluxes associated with a 100 km wide ice stream are
 81 slightly smaller than the 180 km wide ice stream. In both regional model simulations
 82 the upper mantle viscosity was set to 0.4×10^{21} Pa s with sea level 50 m lower than
 83 today. The reference flowline model used in simulations in the text is shown in black.
 84 Ocean forcing corresponds to pulses at 1 ka and 8 ka.



86 **Figure S12** Effect of sea level variations on simulated Heinrich Events using a re-
 87 gional model. Panel **a** shows the deepest portion of the sill for the regional model and
 88 width averaged sill for the flowline model. Panels **b-d** show width averaged speed,
 89 change in terminus position and calving flux. The reference flowline model is shown
 90 in black (sea level 50 m lower than today). We obtain broadly similar results when we
 91 assume sea level rise (SLR) is 50 m and 100 m below present. In regional model sim-
 92 ulations the upper mantle viscosity was set to 0.4×10^{21} Pa s. The flowline model was
 93 obtained using the same parameters as in the main text. Ocean forcing corresponds
 94 to pulses at 1 ka and 8 ka.



96 **Figure S13** Effect of loading model on Heinrich Events computed using a regional
 97 model and flowline model. The regional model uses an upper mantle viscosity $\eta_m =$
 98 0.4×10^{21} Pa s. The flowline model uses an upper mantle viscosity $\eta_m = 0.225 \times 10^{21}$
 99 Pa s. The 1D loading for the regional model was computed by width averaging the
 100 ice thickness. The 2D loading for the regional model was computed assuming no load
 101 outside of the regional model domain. Panel **a** shows the average sill depth (dashed
 102 line) and deepest portion of the sill for the regional models with the width-averaged sill
 103 depth used in the flowline model. Panels **b-d** show width-averaged speed, change in
 104 terminus position and calving flux for the regional model simulations along and flowline

¹⁰⁵ model. Ocean forcing corresponds to pulses at 1 ka and 8 ka.

2 Supplementary Table

Table S1: Parameters used in the model

parameter	description	value	units
ρ	Density of ice	900	kg/m ³
ρ_w	Density of water	1028	kg/m ³
g	Acceleration due to gravity	9.81	m/s ²
B	Ice softness	1.8×10^8	Pa s ^{1/3}
β	Sliding law coefficient	1.5×10^6	Pa (m/s) ^{-1/3}
τ_c	Yield strength of ice	200	kPa
μ	Coefficient of friction	0.0	-
n	Flow law exponent	3	-
p	Sliding law exponent	3	-
\dot{a}	Accumulation rate	0.2	m/a
H_l	Lithospheric thickness	133	km
E	Young's modulus of lithosphere	1.8×10^{11}	Pa
ν	Poisson's ratio of lithosphere	0.29	-
η_m	Viscosity of upper mantle	0.225×10^{21}	Pa·s

3 Supplementary Methods

3.1 Ice dynamics model overview

We evaluated our hypothesis using two models. The first model—and the workhorse of our simulations—consists of a width averaged ‘flowline’ model including an idealized triangular ice sheet connected to a channel (Figure S1). The flowline model, described in section 3.2.1, is computationally cheap allowing us to run multiple simulations for the entire 120 ka duration of the previous glacial period. Furthermore, flowline models have demonstrated an ability to resolve calving front migration associated with outlet and tidewater glacier retreat¹⁵. Flowline models are appropriate for channelized flow where the velocity is primarily directed down channel, a situation that is realistic for the Hudson Strait and are able to numerically accurately resolve calving front motion using a moving grid transformation. However, flowline models are essentially two-dimensional and are therefore unable to resolve cross-channel variations in bed topography and their effects on ice dynamics. To assess the sensitivity of our simulations to a more realistic bathymetry, we also constructed a regional model that simulates the entire catchment basin of the Hudson Strait Ice Stream. This model, described in section 3.2.2, is much more computationally expensive and this limits our simulations to shorter periods. We use this model to assess the sensitivity of our model simulations to a suite of parameters, including relative sea level, upper mantle viscosity and the assumed channel width. The regional model also allows us to assess the effect of three-dimensional loading on isostatic adjustment, something that is not possible with the flowline model. Both models require the specification of the catchment basin, which we describe next.

3.2 Geometry and Model Initialization

We selected a centerline profile extending from the center of the Last Glacial Maximum Laurentide Ice Sheet (the ice divide) to the continental shelf, passing through the center of the Hudson Strait as deduced from the ICE-5G model³¹ (Figure S2). The Hudson Bay dome of the Laurentide Ice Sheet is roughly circular with a diameter of 1250 km in the ICE-5G LGM ice model. We (crudely) approximate the drainage basin of the Hudson Straight Ice Stream as a triangle with a ‘base’ (at $x = 0$) and ‘height’ (from $x = 0$ to channel mouth) of 1242 km. This is connected to an idealized channel 180 km wide. We use this geometry to construct a flowline width that approximates the catchment area and flux of ice feeding the Hudson Strait Ice Stream (Figure S1). The model is initialized with the steady state profile of an ice sheet reaching from the ice divide to the channel entrance with a bed profile beginning with the modern topography from ICE-5G, but allowed to reach equilibrium with the ice sheet. The resulting flowline bed topography is a caricature of the actual topography, which has a much higher sill across portions of the channel mouth and a deep v-shaped channel behind the sill. We also perform simulations using a regional model (section 3.2.2) which has more realistic bathymetry across the entire channel, including the v-shaped channel and sill. The regional model consists of the same basin geometry, but includes the bed topography across the entire channel instead of the width-averaged version from ICE-5G. Because the regional model approach requires higher resolution, we obtained higher resolution topography from bathymetry from ETOPO. We also experimented with GEBCO bathymetry and found little meaningful difference in model results.

3.2.1 Flowline model

Our flowline model is based on the depth-integrated flow of a rapidly sliding ice sheet confined to a channel, a type of model commonly used to study the evolution of Greenland's outlet glaciers¹⁵. There is significant geologic evidence to support a rapidly sliding ice stream draining the Laurentide Ice Sheet through the Hudson Strait during the last glacial interval^{33–35} making this model an appropriate approximation. Denoting the glacier width by W and thickness by H , elevation of the ice sheet surface above sea level by h , horizontal ice sheet velocity by u and horizontal position by x , then balancing depth-integrated forces requires:

$$4 \frac{\partial}{\partial x} \left(H \eta \frac{\partial u}{\partial x} \right) - \beta u^{1/p} - 2B ([n+2]/W)^{1/n} \frac{H}{W} u^{1/n} = \rho g H \frac{\partial h}{\partial x}, \quad (\text{S.1})$$

where, ρ , g , β , B , n , and p are defined in Table S1. η is the effective viscosity and is defined as:

$$\eta = \frac{B}{2} \left[\left(\frac{\partial u}{\partial x} \right)^2 + \epsilon^2 \right]^{\frac{1}{2n}-1}, \quad (\text{S.2})$$

with ϵ a small regularization parameter needed to ensure the viscosity remains finite for vanishing strain rates. The second and third terms in Equation (S.1) represent the effect of friction along the bed and walls, respectively. Resistance due to sliding along the bed is controlled by the parameters β and p , whereas lateral shear is entirely parameterized in terms of the softness of ice (B), ratio of ice thickness to width (H/W) and flow law exponent (n)³⁶. We adopt a constant softness appropriate for -20°C cold ice (Table S1).

For simplicity, we also adopt a Weertman style sliding law and set $p = n = 3$. More complex sliding laws that include effective pressure at the bed, treat the subsurface as a perfect plastic material or include spatially variable coefficient of friction are also possible. However, the Weertman type sliding law is reasonable over a wide spectrum of subglacial substrates^{37–40} and given the idealized nature of our numerical experiments and lack of observational data to

constrain basal friction, we have little reason to prefer a more elaborate sliding law over the commonly used Weertman sliding law. The coefficient in the sliding law is highly uncertain. We adopt a sliding coefficient that gives us an ice sheet profile broadly similar to the ice thickness predicted by ICE-5G at the last glacial maximum (Table S1). This results in basal drag comparable to that seen in Greenland outlet glaciers^{41,42}.

In addition to Equation (S.1), mass conservation requires:

$$\frac{\partial H}{\partial t} + \frac{1}{W} \frac{\partial (WHu)}{\partial x} = \dot{a}, \quad (\text{S.3})$$

where \dot{a} represents the surface accumulation rate in ice equivalent (units of length per unit time) and ablation is represented as negative accumulation. We assume accumulation is spatially constant across the entire ice sheet, a reasonable approximation for most ice sheets.

The origin of our model at $x = 0$ represents an ice divide, whence symmetry requires:

$$\frac{\partial h}{\partial x} = 0, \quad u = 0. \quad (\text{S.4})$$

At the calving front where $x = L(t)$, Equation (S.1) is solved subject to a dynamic boundary condition:

$$4\eta H \frac{\partial u}{\partial x} = \rho g \frac{H^2}{2} - \rho_w g \frac{D^2}{2}, \quad x = L(t), \quad (\text{S.5})$$

where ρ_w denotes the density of sea water and D denotes the distance from the ocean surface to the bottom of the ice. Values for all parameters used in the model are compiled in Table S1.

Provided the first term in Equation (S.1) is small compared to the sum of the second and third terms, we can make the approximation that away from the calving front

$$-\beta u^{1/n} - 2B \left(\frac{n+2}{W} \right)^{1/n} \frac{H}{W} u^{1/n} = \rho g H \frac{\partial h}{\partial x}. \quad (\text{S.6})$$

¹⁸³ Substituting Equation (S.6) into the mass conservation equation, Equation (S.3), provides a
¹⁸⁴ diffusion equation for ice thickness:

$$\frac{\partial H}{\partial t} = \frac{1}{W} \frac{\partial}{\partial x} \left(\Gamma \frac{\partial h}{\partial x} \right) + \dot{a}, \quad (\text{S.7})$$

¹⁸⁵ with:

$$\Gamma = \frac{\left(\frac{\rho g}{\beta} \right)^{1/n} W H \left(H \left| \frac{\partial h}{\partial x} \right| \right)^{1/n-1}}{\left[1 + \frac{2HB}{\beta W} \left(\frac{n+2}{W} \right)^n \right]}. \quad (\text{S.8})$$

¹⁸⁶ The denominator in Equation (S.8) represents a slight generalization of the usual diffusivity in
¹⁸⁷ that it accommodates a small amount of lateral shear. If H/W is small, as it is for the Hudson
¹⁸⁸ Strait Ice Stream, to a good approximation:

$$\Gamma \approx \left(\frac{\rho g}{\beta} \right)^{1/n} W H \left(H \left| \frac{\partial h}{\partial x} \right| \right)^{1/n-1}, \quad (\text{S.9})$$

¹⁸⁹ corresponding to the rapidly sliding ice sheet model used by previous researchers^{43,44}. With the
¹⁹⁰ exception of the lateral shear term, this is the form of the boundary layer problem initially de-
¹⁹¹ rived for marine ice sheets⁴³. Defining a characteristic length of the ice sheet domain $L_0 \approx 2400$
¹⁹² km, accumulation scale a_0 , the ratio of resistance to deformation due to longitudinal membrane
¹⁹³ stresses and resistance from friction at the bed is given by the non-dimensional number Δ :

$$\Delta = B \left[\frac{a_0}{(\rho g)^n} \beta^{n+1} L_0^{(1/n+1)(1+n)} \right]^{1/(1+2n)}. \quad (\text{S.10})$$

¹⁹⁴ The boundary layer approximation is valid provided $\Delta \ll 1$. For the parameters in Table
¹⁹⁵ S1, $\Delta \sim 0.01$, suggesting that the boundary layer approximation is indeed appropriate. This
¹⁹⁶ approximation neglects vertical shear deformation. The effect of vertical shear can easily be
¹⁹⁷ incorporated into the model, but our investigations found that, as expected, vertical shear had
¹⁹⁸ little effect on model results.

3.2.2 Regional model

²⁰⁰ The three dimensional version of the flowline boundary layer approximation can be written in
²⁰¹ the form:

$$\frac{\partial H}{\partial t} = \frac{\partial}{\partial x} \left(\Gamma' \frac{\partial h}{\partial x} \right) + \frac{\partial}{\partial y} \left(\Gamma' \frac{\partial h}{\partial y} \right) + \dot{a} \quad (\text{S.11})$$

²⁰² with

$$\Gamma' = \left(\frac{\rho g}{\beta} \right)^{1/n} H \left(H \left[\left(\frac{\partial h}{\partial x} \right)^2 + \left(\frac{\partial h}{\partial y} \right)^2 \right] \right)^{\frac{1}{2n}-\frac{1}{2}}. \quad (\text{S.12})$$

²⁰³ Equation (S.11) forms the basis for our regional model. For the regional model, in addition to
²⁰⁴ the symmetry condition at the ice divide, we impose a no inflow boundary condition at the sides.
²⁰⁵ The no-inflow condition, consistent with the assumption that our model domain covers the
²⁰⁶ catchment basin of the Hudson Strait Ice Stream, is enforced by insisting that the surface slope
²⁰⁷ normal to the domain walls vanishes. We again tested the role of vertical shear deformation, but
²⁰⁸ found that vertical shear had little effect on our simulations.

209 3.2.3 Moving boundary transformation and model numerics

²¹⁰ We adopt a moving grid to track the terminus. Defining,

$$\xi = \frac{x}{L(t)}, \quad t^* = t, \quad (\text{S.13})$$

introduces a coordinate transformation that maps the interval $0 \leq x \leq L(t)$ into the interval
 $0 \leq \xi \leq 1$. The variable t^* is introduced to distinguish between partial derivatives obtained

holding x or ξ constant. Application of the chain rule leads to the relations:

$$\frac{\partial}{\partial x} = \frac{1}{L} \frac{\partial}{\partial \xi} \quad (\text{S.14})$$

$$\frac{\partial}{\partial t} = \frac{\partial}{\partial t^*} - \frac{\xi}{L} \frac{dL}{dt^*} \frac{\partial}{\partial \xi} \quad (\text{S.15})$$

Using these, the mass conservation equation, Equation (S.3), becomes:

$$\frac{\partial H}{\partial t^*} - \frac{\xi}{L} \frac{dL}{dt^*} \frac{\partial H}{\partial \xi} + \frac{1}{L} \frac{\partial (Hu)}{\partial \xi} = \dot{a} \quad (\text{S.16})$$

²¹¹ Similar transformations apply to the remaining equations.

²¹² We solve the boundary layer problem for the flowline model using a pseudo-spectral
²¹³ method on a Chebyshev grid⁴⁵ with 200 quadrature points and an implicit time step. Termination
²¹⁴ advance/retreat is dealt with using an explicit time step. This necessitated using a relatively
²¹⁵ small time step of 1 year. The advantage of the spectral method is that the tight grid spacing
²¹⁶ near the boundaries naturally resolves the boundary layer without the need to switch to a higher
²¹⁷ resolution grid near the margin. We checked the numerical algorithm by comparing to steady-
²¹⁸ state solutions for ice sheet profiles obtained analytically for a flat bed or by quadrature for an
²¹⁹ arbitrary bed shape. Results are insensitive to changing the grid spacing or time step, suggesting
²²⁰ numerical convergence.

²²¹ For the regional model, we applied a similar spectral method to both horizontal coordi-
²²² nates after first applying an additional coordinate transformation that mapped the irregular do-
²²³ main into a rectangular domain. For most simulations we used 100 points in the along channel
²²⁴ direction and 11 points in the transverse to channel direction. We did not perform as extensive
²²⁵ convergence tests, but generally found that increasing resolution by 50% had little effect on
²²⁶ simulation results. We also needed to decrease the time step to a quarter year to obtain accurate

²²⁷ solutions. We still need to specify rate at which the terminus advances and retreats and this
²²⁸ requires a parameterization of calving, which we discuss next.

²²⁹ 3.3 Parameterization of calving

²³⁰ 3.3.1 Theory of calving parameterization

²³¹ Our approach to calving builds on recent studies that suggest that the maximum terminus thick-
²³² ness is limited by the yield strength of ice^{19,20}. Following Bassis and coauthors^{19,20}, we define
²³³ the yield strength of ice using a Coulomb type-failure law of the form $\tau_y = \tau_c + \mu N$, where
²³⁴ τ_c is the yield strength, μ is the coefficient of friction and $N = \rho g H - \rho_w g D$ is the effective
²³⁵ normal pressure. The depth integrated stress at the calving front must be less than the depth
²³⁶ averaged yield strength lest catastrophic cliff failure occurs. Applying a force balance at the
²³⁷ calving front, the maximum ice thickness permitted is given by¹⁹:

$$H_c = \frac{2\tau_c}{\rho g(1-2\mu)} + \sqrt{\left(\frac{2\tau_c}{\rho g}[1-2\mu]\right)^2 + \frac{\rho_w}{\rho} D^2}, \quad (\text{S.17})$$

²³⁸ for a given water depth D . Terminus thickness is constrained such that $H(x = L) \leq H_c$.

²³⁹ Previous ice sheet models have enforced this condition semi-empirically by assuming that
²⁴⁰ the calving rate increased with increasing near terminus ice thickness^{21,46,47} or by explicitly
²⁴¹ modeling the shear failure of ice²⁰. Here we adopt a slightly different approach. Taking the
²⁴² material derivative of Equation (S.17) with respect to time we find that

$$\frac{\partial H}{\partial t} + \frac{dL}{dt} \frac{\partial H}{\partial x} \leq \frac{\partial H_c}{\partial t} + \frac{dL}{dt} \frac{\partial H_c}{\partial x}, \quad (\text{S.18})$$

where the term dL/dt represents the rate of advance of the terminus (negative for retreat). The maximum ice thickness H_c has a time dependence because isostatic adjustment and changing sea level leads to time variation in water depth D . However, in all calculations performed here, the contribution from the time rate of change of bed topography is small enough that we can neglect the time rate of change of H_c , leading to the simpler equation:

$$\frac{\partial H}{\partial t} + \frac{dL}{dt} \frac{\partial H}{\partial x} \leq \frac{dL}{dt} \frac{\partial H_c}{\partial x}. \quad (\text{S.19})$$

The mass continuity equation, Equation (S.3) remains valid at the terminus ($x = L$), giving:

$$\frac{\partial H}{\partial t} + u \frac{\partial H}{\partial x} + H \frac{\partial u}{\partial x} = \dot{a}. \quad (\text{S.20})$$

Combining Equations (S.19) and (S.20) to eliminate the time derivative of ice thickness, yields:

$$\frac{dL}{dt} \geq \frac{\dot{a} - u \frac{\partial H}{\partial x} - H \frac{\partial u}{\partial x}}{\left(\frac{\partial H_c}{\partial x} - \frac{\partial H}{\partial x} \right)}, \quad x = L. \quad (\text{S.21})$$

This evolution equation is analogous to the expression derived for the migration of the grounding line of a marine ice sheet^{43,44}. However, Equation (S.21) provides a lower bound on the rate of terminus advance and can be used to describe a range of calving scenarios depending on the yield strength. For example, if H_c is given by the flotation condition then the equality implied by Equation (S.21) exactly reproduces the model for grounding line migration derived previously⁴³. The advantage of Equation (S.21) is that it provides a lower-bound on the rate of terminus advance, or, equivalently, an upper bound on the calving rate for a fixed yield strength. Moreover, in contrast to empirical formulations^{21,46,47}, once the yield strength is set, the terminus position and calving flux are then entirely determined without the need for additional parameters needed in the empirical formulation used by others^{21,47}.

3.3.2 Calibration of calving parameterization

To determine the appropriate yield strength (τ_y), we look to observations of water depth and ice thickness from many modern glaciers¹⁹ (Figure S3). We find that the combination of $\tau_c = 200$ kPa and $\mu = 0$ fits the observations reasonably well. With this fit, the rate of advance is entirely constrained with no additional parameters. Increasing the yield strength above 200 kPa increases the calving rate leading to faster retreat and slower advance, but changing the yield strength does not qualitatively change the results. We caution that an important limitation of our parameterization of calving is that our model only applies to grounded glaciers. Formation of freely floating ice tongues and ice shelves is prohibited. This is only a minor limitation for our study because we focus on tidewater-type calving instabilities and there is little evidence of a semi-permanent ice tongue in the region (see Supplementary Discussion)

In the flowline model, we need only enforce Equation (S.21) at the calving front. In the regional model, the above parameterization could be applied at every point along the calving front. However, because icebergs have finite width and for numerical convenience, we enforce a width averaged version of Equation (S.21) in which we compute the rate of terminus advance for every point along the calving front and then allow the entire terminus to advance or retreat at the same rate based on the median rate of advance and retreat. We also investigated computing the advance rate based on the average ice thickness, terminus velocity and bed topography and found similar results.

3.4 Submarine melt parameterization

280 The ice dynamics model also requires specifying the effect of submarine melting along the
 281 calving front (Figure S4). Unlike ‘full’ Stokes flow models that do not depth average, in depth
 282 integrated approximations like the ones used here, we cannot specify a submarine melt rate
 283 directly. The rate of ice lost over the calving front per unit width, Q_m (units of m^2/a) is given
 284 by:

$$Q_m = \dot{m}_f D \quad (\text{S.22})$$

285 where \dot{m}_f denotes the average submarine melt rate (units of m/a) along the submerged por-
 286 tion of the calving face and D , as before, denotes the water depth. Previous studies^{21,47} have
 287 sought to apply this mass loss by removing ice from the top surface as an effective (negative)
 288 accumulation rate, averaged over a grid cell of size Δx :

$$\dot{a}_{eff} = -\frac{\dot{m}_f D}{\Delta x}, \quad (\text{S.23})$$

289 This method is effective for coarse scale continental ice sheet models, but predicts an effective
 290 melt rate that diverges as the grid size Δx becomes small. This results in models that fail to
 291 converge numerically. Instead, we assume that the effective melt rate is concentrated in a region
 292 that is approximately one ice thickness (H) in size, instead of over one grid cell (Δx) (Figure
 293 S4). We assume submarine melt corresponds to an effective (surface) accumulation rate that is
 294 largest at the terminus and decreases to zero at a distance of one ice thickness. Balancing the
 295 total mass lost then requires:

$$\dot{a}_{eff} = \begin{cases} -2 \left(1 - \frac{L-x}{H}\right) \frac{D}{H} \dot{m}_f, & x > L-H \\ 0, & x \leq L-H \end{cases} \quad (\text{S.24})$$

This approximation reduces to the approximation used by others^{21,47} when the grid spacing is
297 large compared to the ice thickness. Physically, this parameterization has the effect of increasing
298 the surface slope of the glacier near the calving front, as has been observed on existing
299 glaciers⁴⁸. We have experimented with different forms of the shape function, including (1) a
300 constant thinning rate over 1 ice thickness and (2) an exponential decrease in thinning rate with
301 e-folding distance 1 ice thickness. These alter the sensitivity of the ice sheet to the magnitude
302 of melt rate (and therefore the magnitude of ocean forcing), but all yield qualitatively similar
303 results.

304 The amplitude of the submarine melt was related to ocean forcing using the rough approx-
305 imation that a $1^{\circ}C$ increase in thermal forcing corresponds to a submarine melt rate increase of
306 100 m/a. This is a very conservative estimate of submarine melt rate¹⁶. Observations of tide-
307 water glaciers suggest much higher melt rates per degree of thermal forcing are possible when
308 ample freshwater discharge at the bottom of the glacier creates a rapidly rising buoyant plume⁴⁸.
309 We also ignore the effect of pressure and salinity on thermal forcing. Including pressure would
310 increase the submarine melt rate when the terminus retreats into deeper water. However, re-
311 treat into deeper water usually occurs simultaneously with increased iceberg production and the
312 melting icebergs might lead to a decrease in the temperature of the water column.

3.5 Isostatic adjustment model

314 The final component of our model is the isostatic adjustment model. The most sophisticated
315 models of isostatic adjustment are global models based on a self-gravitating, spherical, vis-
316 coelastic multi-layer Earth (SVGE) models with a self-consistent sea level equation^{49,50}. Given

317 the fact that our ice dynamics model only represents a portion of the ice sheet and these models
 318 require us to specify the global distribution of ice sheets, we employed a simpler model based
 319 on a half-space viscous mantle overlain by an elastic lithosphere^{24,49}. Denoting the vertical
 320 displacement of the surface by w , viscosity of the mantle by η_m this model is described by the
 321 single partial differential equation²⁴:

$$2\eta_m |\nabla| \frac{\partial w}{\partial t} + \rho_r gw + K\nabla^4 w = \sigma_{zz} \quad (\text{S.25})$$

322 where σ_{zz} denotes the load on the lithosphere, ρ_r denotes the density of the mantle and

$$K = \frac{E^3 H_l}{12(1 - \nu^2)}, \quad (\text{S.26})$$

323 is the lithospheric rigidity with elastic thickness H_l , Young's Modulus E and Poisson's ratio
 324 ν . The load σ_{zz} , includes contributions due to both ice and ocean loading. We focus on a
 325 single mantle viscosity, but this model can also be extended to include a two-layer mantle
 326 corresponding to an upper mantle and lower mantle⁴⁹.

The pseudo-differential operator $|\nabla|$ is most easily defined in the Fourier Transform do-
 328 main. Denoting the wavenumber by κ , the operator $|\nabla| = \sqrt{\kappa_x^2 + \kappa_y^2}$. Ideally, we would solve
 329 Equation S.25 with global ice loading. In practice, we know little about the loading outside of
 330 our model domain rendering this approach unfeasible. Instead, we define two extreme load-
 331 ing configurations. In the first, which we call 1D loading, we width average the load and set
 332 $\kappa_y = 0$, whence $|\nabla| \approx |\kappa| = \sqrt{\kappa_x^2}$. This approximation, however, assumes that the load ex-
 333 tends infinitely far in the transverse to flow direction. Our flowline model is a width averaged
 334 model and width integrated loading is the only information we have available. For the regional
 335 model, in addition to width averaging, we can also consider the two dimensional loading field,
 336 but need to extrapolate to find the loading outside of our model domain. We do this by assuming
 337 zero load outside of the model domain, which we call 2D loading. These two extremes bracket

338 the more realistic loading situation. Our goal is to use Equation S.25 to provide a reasonable
339 spectrum of relaxation times and amplitudes of isostatic adjustment and investigate the extent
340 to which different loading assumptions influence our results.

341 We ignore gravitational effects on near-field sea level²² because the scale of eustatic sea
342 level rise due to ice loss during a Heinrich Event is only \sim 1-2 m. We estimate a load this size
343 would lead to a \sim 10 m drop in local sea level, which is small compared to the uncertainty in
344 our bed topography. We take glacial sea level changes due to continental ice accumulation into
345 account by lowering eustatic sea level by 50 m, which is appropriate for Marine Isotope Stage 3
346 and 4 when the majority of Heinrich Events occur, but also perform sensitivity studies to larger
347 and smaller changes in sea level.

348 Figure S5 shows the relaxation time spectrum for an elastic lithosphere overlying a con-
349 stant viscosity mantle and an elastic lithosphere overlying a two-layer mantle with constant
350 upper and lower mantle viscosities. The effect of the lower mantle is most prominent for wave-
351 lengths greater than 1000 km. However, our ice sheet in its most extended position is only
352 2000 km long and we are unable to fully resolve wavelengths larger than \sim 1000 km, making
353 it relatively insensitive to the lower mantle. For this reason, we restrict our models to an elastic
354 lithosphere overlying a single viscosity (upper) mantle for all simulations.

355 Our implementation of the model is similar to that proposed by Bueler et al.²⁴. We con-
356 sider an equally spaced grid that is 4000 km long, roughly double the size of the ice sheet at its
357 largest extent. We linearly interpolate from the irregular spaced computational grid of the ice
358 sheet model to the regular grid used for the isostatic adjustment model at every time step. We
359 then fit the bed topography with a smooth spline to interpolate back to the irregular grid. The
360 larger domain size for the isostatic model is needed to minimize edge effects associated with

361 the Fourier Transform. We assume reflection symmetry across $x = 0$ to extend the loading in
362 the negative x-direction away from the ice divide (extending the total domain size to 8000 km).
363 This more realistically accounts for loading at the ice divide and within the catchment basin and
364 has little effect on the bed topography within the channel. For the flowline model, we used 2048
365 points, but doubling the number of points had little effect on the results. For the regional model,
366 with fully 2D loading, we used a square domain with 1024 points in both horizontal direction.

3.6 Ocean Forcing

3.6.1 Constraints on subsurface warming from proxies and models

369 We drive the model with a prescribed ocean thermal forcing, delivered by warm subsurface wa-
370 ters to the calving front. Evidence supporting subsurface warming preceding Heinrich Events
371 is many-fold. Subsurface warming occurs as the result of reduced Atlantic Meridional Over-
372 turning Circulation (AMOC), as has been shown in many hosing experiments that force a re-
373 duction in the AMOC by artificially dumping freshwater across the North Atlantic and ob-
374 serve the resulting subsurface warming anomalies^{51–53}. In these experiments, as the AMOC
375 becomes weaker, subsurface waters increasingly warm across the North Atlantic, including in
376 the Labrador Sea. In one hosing experiment initiated with freshwater placed across a band from
377 50–70°N in the North Atlantic, Fluckiger et al.⁵¹ find that subsurface warming at the channel
378 mouth of the Hudson Strait was even amplified relative to the outlet of the Labrador Sea. Sub-
379 surface warming has been seen in proxy records in the Nordic Seas during all stadial phases
380 (Heinrich or non-Heinrich)⁵⁴, and at the outlet of the Labrador Sea during Heinrich stadials⁸.
381 The closest evidence of subsurface warming comes from a sediment core at the outlet of the

382 Labrador Sea⁸. The magnitude of warming observed in the Labrador Sea is approximately 1-3
383 °C during four Heinrich stadials (only stadials measured, study had limited sampling)⁸. We
384 use this observation to constrain the magnitude of subsurface thermal forcing applied to our ice
385 model.

386 Sediment core records document strong reductions in the AMOC during Heinrich stadials⁵⁵⁻⁵⁸
387 and weaker reductions during non-Heinrich stadials⁵⁵. This could indicate that subsurface
388 warming during Heinrich stadials was enhanced relative to non-Heinrich stadials. However,
389 it is also possible that the larger and longer perturbation to the AMOC during Heinrich stadials
390 was at least partially the *result* of the increased freshwater input caused by the Laurentide col-
391 lapse. For this reason, we choose to treat all DO stadials equally, and create an ocean forcing
392 function with identically-sized warming pulses during each DO stadial phase. By treating all
393 DO stadials equally, we present the most severe test of our model.

3.6.2 Specification of forcing

395 The basic pulse shape that we used for simulations is a sinusoidal shaped pulse with half-period
396 t_d and maximum warming T_{max} . Each sinusoidal pulse is based on the timing of the DO event
397 onset (warming in Greenland $\delta^{18}O_{ice}$ record). Reduced AMOC conditions exist during the sta-
398 dial phase, initiating subsurface warming. Once the DO event occurs, the AMOC reinvigorates
399 and subsurface temperature anomalies dissipate.

Denoting the ocean thermal forcing associated with the i th DO event by T_o^i and the timing

of the i th DO event by t_i , the ocean thermal forcing has the form of a sinusoid:

$$T_o^i = \begin{cases} T_{max} \left| \sin \left(2\pi \frac{(t - t_i)}{2t_d} \right) \right| & t_i - t_d \leq t \leq t_i, \\ 0 & \text{otherwise.} \end{cases} \quad (\text{S.27})$$

⁴⁰⁰ The total rate of warming when pulses overlap is obtained by summing the contributions from
⁴⁰¹ individual DO cycles:

$$\Delta T_o = \sum_i T_o^i. \quad (\text{S.28})$$

⁴⁰² The exact timing of the DO events was taken from the updated Greenland ice core chronology²⁹.
⁴⁰³ The age model for the sediment core MD95-2025, which documents many Heinrich and Heinrich-
⁴⁰⁴ like Events at the mouth of the Labrador Sea (Figure 2g)²⁸ was updated to the latest ice core age
⁴⁰⁵ model using a published conversion software⁵⁹ to facilitate direct comparison between model
⁴⁰⁶ and data.

⁴⁰⁷ We set the magnitude of the pulses (T_{max}) based on paleo-subsurface-ocean tempera-
⁴⁰⁸ ture data⁸, which suggests intermediate water temperature increased by 1-3°C. This is roughly
⁴⁰⁹ comparable to the recent increased thermal forcing experienced by Pine Island and Thwaites
⁴¹⁰ Glaciers^{60,61} and small compared to the increased thermal forcing experienced by many Green-
⁴¹¹ land and Alaska outlet glaciers^{16,62,63}. For our base experiments, we assumed that warming
⁴¹² occurred over 1.2 ka ($t_d \equiv 1.2$ ka), a time period roughly comparable to the time scale of the
⁴¹³ overturning circulation. This choice limits the overlap of adjacent warming pulses for all but
⁴¹⁴ the most closely spaced DO events.

⁴¹⁵ The depth to which the subsurface warming rises is uncertain. We set the depth of subsur-
⁴¹⁶ face warming at 250 meters below the surface based on modern mixed layer depths in Greenland
⁴¹⁷ fjords in winter^{62,64,65} and the depth of modeled subsurface warming from hosing experiments⁵¹.

⁴¹⁸ We further assume that the transition from warm to cold surface layers occurs over a finite trans-
⁴¹⁹ sition zone

$$T(z) = \frac{\Delta T_0}{2} \left[1 + \tanh \left(\frac{z - l}{\ell} \right) \right], \quad (\text{S.29})$$

⁴²⁰ where z represents the depth beneath the surface of the water, l denotes the depth to which
⁴²¹ the subsurface warming penetrates and the transition length ℓ was set to 10 m. We conduct
⁴²² sensitivity experiments in which we vary the depth of subsurface warming and find the same
⁴²³ qualitative behavior for a range of subsurface warming depths (Figure S9).

⁴²⁴ We use a warming pulse of equal magnitude for all DO stadials except the one preceding
⁴²⁵ DO 13, which appears in the Greenland $\delta^{18}\text{O}_{ice}$ record at about 50 ka as a small blip following
⁴²⁶ the long recovery from DO 14^{29,30}. Due to the long time interval between DO 14 and DO 13,
⁴²⁷ a Heinrich Event is triggered in our model at DO 13, one stadial phase too early. If the warm
⁴²⁸ pulse corresponding to DO 13 is eliminated, the model correctly reproduces the timing of the
⁴²⁹ remaining Heinrich Events, beginning with H5 prior to DO 12. We consider omitting the DO
⁴³⁰ 13 warming pulse to be justified because the shape of DO 13 is unlike any of the other DO
⁴³¹ events. Specifically, DO 13 is not preceded by a typical stadial phase, in that the Greenland
⁴³² $\delta^{18}\text{O}_{ice}$ record does not reach full stadial values or stay low for a sufficient length of time to
⁴³³ allow significant ocean warming.

4 Supplementary Discussion

435 4.1 Flowline model sensitivity

436 4.1.1 Sensitivity of flowline model to accumulation rate

437 Accumulation rate is determined by the difference between rate of mass added through snowfall
438 and rate of mass removed by surface melting. Past accumulation rates for the Laurentide Ice
439 Sheet are poorly constrained, but we select values consistent with modern and estimated glacial
440 Greenland accumulation rates. The selected accumulation rate is constant over the whole ice
441 sheet. We examined the effect of varying the accumulation rate on the minimum ocean forcing
442 T_{max} that could trigger Heinrich Events (Figure S6). Decreasing the accumulation rate reduces
443 the threshold of thermal forcing needed to trigger Heinrich Events, leading to ice sheets more
444 susceptible to small perturbations in ocean warming. This is a consequence of the decreased
445 flux feeding the ice stream. We also see a trade-off between accumulation rate and upper mantle
446 viscosity (Figure S7). For example, when the accumulation rate is too low, the ice sheet cannot
447 advance fast enough to trigger Heinrich Events at the right times and the mean interval between
448 Heinrich Events (the recurrence interval) increases. This effect is amplified by a larger upper
449 mantle viscosity. Conversely, as the accumulation rate increases, the ice sheet can advance
450 more rapidly, decreasing the recurrence interval. For the two viscosities tested, we find a broad
451 range of accumulation rates for which our model produces Heinrich Events with about the right
452 recurrence intervals (\sim 7-10 ka).

4.1.2 Sensitivity of flowline model results to ocean forcing

454 Employing different pulse shapes for ocean forcing, including triangular pulses and square
455 pulses, did not significantly impact on our results. Varying pulse magnitude (T_{max}) also had
456 a negligible effect on the timing of Heinrich Events, as long as the pulse amplitude exceeded
457 a minimum threshold (Figure S6). Using a much larger thermal forcing, a Heinrich Event was
458 sometimes triggered one stadial earlier than observed for closely spaced DO events. Increasing
459 the duration of pulses had little effect on early Heinrich Events when DO events were
460 infrequent, but during the later glacial when DO events were more closely spaced, this led
461 to a near continuous ocean forcing that prevented full re-advance of the ice sheet between DO
462 events. Pulse durations significantly less than 750 a required a much larger ocean forcing signal
463 to trigger Heinrich Events.

4.1.3 Sensitivity of flowline model results to upper mantle viscosity

465 To further test the sensitivity of our results to the assumed viscosity structure, we performed a
466 set of experiments at fixed accumulation rate where we varied the upper mantle viscosity for two
467 scenarios (two sets of model parameters) (Figure S8). Both scenarios can successfully repro-
468 duce the timing of all Heinrich Event for a specific range of viscosities that is broadly consistent
469 with accepted solid Earth structure^{25,66}. For upper mantle viscosities of $\sim 0.2\text{--}0.4 \times 10^{21}$ Pa s,
470 Heinrich Events were produced at roughly the correct recurrence interval (5-10 ka for H1-H6,
471 longer for older Heinrich Events). For viscosities larger than $\sim 0.4 \times 10^{21}$ Pa·s, it takes longer
472 for the ice stream to re-advance and depress the bed, resulting in more widely spaced events.
473 For viscosities lower than 0.2×10^{21} Pa s, the model produced only small Heinrich-like Events

474 coincident with each melt pulse, with retreat often less than a few 100 km followed by rapid
475 re-advance. Retreat of this magnitude is impressive for modern glaciers, but too small to gener-
476 ate the sediment or freshwater flux needed to explain Heinrich Events³. The quantitative effect
477 of changing viscosity is clear in both cases: increasing viscosity lengthens the mean recurrence
478 time—consistent with isostatic rebound setting the time scale of re-advance, and through that,
479 the timing of Heinrich Events.

4.1.4 Sensitivity of flowline model to depth of ocean warming

481 We next examined the sensitivity of the recurrence interval of Heinrich Events to the depth of
482 subsurface warming, assuming constant forcing during all DO events. Figure S9 shows results
483 of this sensitivity test for two upper mantle viscosities with glacial sea levels 50 m and 100
484 m below present. We again see that our model can produce Heinrich Events with recurrence
485 intervals comparable to observations (7-10 ka) for a range of viscosities and subsurface warm-
486 ing depths for both glacial sea level scenarios. If the subsurface warming reaches too close to
487 the surface (depth of warming <100 m), the sill never isolates the ice sheet from the warming.
488 The ice sheet feels every pulse of ocean warming and is prevented from fully advancing unless
489 gaps between pulses are long enough. This is demonstrated by the larger average recurrence
490 intervals at depths of warming less than 100 m from the surface. Our model can still produce
491 Heinrich Events with the correct spacing with subsurface warming at these near-surface depths
492 if the pulses of warming are weaker during non-Heinrich stadials. There is evidence supporting
493 the idea that the magnitude of subsurface warming may have been smaller during non-Heinrich
494 stadials (seen as smaller changes in AMOC strength⁵⁶), but the larger magnitude of AMOC re-
495 duction during Heinrich stadials may in fact be the result of the influx of icebergs and freshwater

⁴⁹⁶ during the Heinrich Event, as opposed to an anomalously large forcing.

4.2 Comparison between flowline model and regional model

4.2.1 Sensitivity of regional model to upper mantle viscosity

⁴⁹⁹ Figure S10 shows a comparison between the flowline model and regional model with upper
⁵⁰⁰ mantle viscosities ranging from $0.225\text{--}0.6 \times 10^{21}$ Pa s. Changing the upper mantle viscosity
⁵⁰¹ affects the rate of re-advance with lower viscosities resulting in quicker re-advance and more
⁵⁰² rapid deepening of the sill. We see that the regional model advances more quickly from its most
⁵⁰³ retreated position. The regional model with a $\sim 0.4 \times 10^{21}$ Pa s upper mantle viscosity has a
⁵⁰⁴ qualitatively similar rate of advance as the flowline model with 0.225×10^{21} Pa s upper mantle
⁵⁰⁵ viscosity.

4.2.2 Sensitivity of regional model to channel width

⁵⁰⁷ Changing the width of the channel portion from 180 to 100 km does not have significant influ-
⁵⁰⁸ ence on the timing of re-advance, but slightly increases the ice velocity during collapse (Figure
⁵⁰⁹ S11 and Supplementary Animation M2 and M3) decreases the calving flux during Heinrich
⁵¹⁰ Events.

4.2.3 Sensitivity of regional model to sea level

512 We also experimented with a range of sea levels. For example, using a glacial sea level equiva-
513 lent to modern ($SLR=0$) as opposed to 50 meters below modern ($SLR = -50$ m) causes a slower
514 re-advance, but again does not change the character of events (Figure S12). The more deeply
515 grounded the ice sheet is beneath sea level, the more sensitive the ice sheet is to ocean forcing.

4.2.4 Sensitivity of regional model to loading geometry

517 Finally, we also used the regional model to examine assumptions about the loading geometry. To
518 compare more directly to the flowline model, a 1D loading was computed for the regional model
519 by width-averaging the ice thickness and then assuming that the loading extended infinitely
520 in the lateral direction. The 2D loading for the regional model was computed assuming no
521 load outside of the regional model domain. These two limits bracket the more likely behavior
522 in which there was some ice outside of the model domain. Figure S13 shows a comparison
523 between these three simulations. For all simulations we see broadly similar patterns in the
524 retreat and advance patterns between all scenarios. These simulations suggest that our model is
525 not sensitivity to the precise form of loading assumed and our flowline model is likely to give
526 realistic results.

Code availability Code is publicly available at <https://github.com/jbassis/pyglacier>.

Data availability We obtained data from the NGRIP ice core from <http://www.iceandclimate.nbi.ku.dk/data>
529 and from MD95-2025 sediment core from <https://doi.pangaea.de/10.1594/PANGAEA.760202>.

5 Supplementary References

31. Peltier, W. Global glacial isostasy and the surface of the ice-age earth: The ice-5g (vm2) model and grace. *Annual Review of Earth and Planetary Sciences* **32**, 111–149 (2004).
32. Bond, G. *et al.* Evidence for massive discharge of icebergs into the North Atlantic ocean during the last glacial period. *Nature* **360**, 245–249 (1992).
33. Krabbendam, M., Eyles, N., Putkinen, N., Bradwell, T. & Arbelaez-Moreno, L. Stream-lined hard beds formed by palaeo-ice streams: A review. *Sedimentary Geology* **338**, 24–50 (2016).
34. Laymon, C. A. Glacial geology of western Hudson Strait, Canada, with reference to Laurentide Ice Sheet dynamics. *Geological Society of America Bulletin* **104**, 1169–1177 (1992).
35. Margold, M., Stokes, C. R. & Clark, C. D. Ice streams in the Laurentide Ice Sheet: Identification, characteristics and comparison to modern ice sheets. *Earth-Science Reviews* **143**, 117–146 (2015).
36. Van der Veen, C. J. *Fundamentals of Glacier Dynamics* (Balkema, 1999).
37. Weertman, J. On the sliding of glaciers. *Journal of Glaciology* **3**, 33–38 (1957).

38. Paterson, W. S. B. *The Physics of Glaciers* (Reed Educational and Professional Publishing Ltd, Oxford, 1994), third edn.
39. Benn, D. I., Hulton, N. R. J. & Mottram, R. H. ‘Calving laws’, ‘sliding laws’ and the stability of tidewater glaciers. *Annals of Glaciology* **46**, 123–130 (2007).
40. Gudmundsson, G. H. Ice-stream response to ocean tides and the form of the basal sliding law. *The Cryosphere* **5**, 259–270 (2011).
41. Van Der Veen, C., Plummer, J. & Stearns, L. Controls on the recent speed-up of jakobshavn isbrae, west greenland. *Journal of Glaciology* **57**, 770–782 (2011).
42. Joughin, I. *et al.* Seasonal to decadal scale variations in the surface velocity of jakobshavn isbrae, greenland: Observation and model-based analysis. *Journal of Geophysical Research: Earth Surface* **117** (2012). F02030.
43. Schoof, C. Marine ice-sheet dynamics. Part 1. The case of rapid sliding. *Journal of Fluid Mechanics* **573**, 27–55 (2007).
44. Schoof, C. Ice sheet grounding line dynamics: Steady states, stability, and hysteresis. *Journal of Geophysical Research* **112** (2007). F03S28.
45. Boyd, J. P. *Chebyshev and Fourier Spectral Methods* (Courier Dover Publications, 2001).

46. Brown, C. S., Meier, M. F. & Post, A. Calving speed of Alaska tidewater glaciers, with applications to Columbia Glacier. *U.S. Geological Survey Professional Paper* **1258-C**, 13p (1982).
47. Pollard, D., DeConto, R. M. & Alley, R. B. Potential Antarctic Ice Sheet retreat driven by hydrofracturing and ice cliff failure. *Earth and Planetary Science Letters* **412**, 112–121 (2015).
48. Motyka, R. J., Dryer, W. P., Amundson, J., Truffer, M. & Fahnestock, M. Rapid submarine melting driven by subglacial discharge, LeConte Glacier, Alaska. *Geophysical Research Letters* **40**, 5153–5158 (2013).
49. Cathles, L. M. *Viscosity of the Earth's Mantle* (Princeton University Press, 1975).
50. Peltier, W. R. The impulse response of a maxwell earth. *Reviews of Geophysics* **12**, 649–669 (1974).
51. Flückiger, J., Knutti, R. & White, J. W. Oceanic processes as potential trigger and amplifying mechanisms for Heinrich events. *Paleoceanography* **21** (2006).
52. Liu, Z. *et al.* Transient simulation of last deglaciation with a new mechanism for Bolling-Allerod warming. *Science* **325**, 310–314 (2009).
53. Zhang, X., Prange, M., Merkel, U. & Schulz, M. Spatial fingerprint and magnitude of changes in the Atlantic meridional overturning circulation during marine isotope stage 3. *Geophysical Research Letters* **42**, 1903–1911 (2015).

54. Rasmussen, T. L. & Thomsen, E. The role of the north atlantic drift in the millennial timescale glacial climate fluctuations. *Palaeogeography, Palaeoclimatology, Palaeoecology* **210**, 101–116 (2004).
55. Elliot, M. *et al.* Millennial-scale iceberg discharges in the Irminger Basin during the last glacial period: Relationship with the Heinrich events and environmental settings. *Paleceanography* **13**, 433–446 (1998).
56. Elliot, M., Labeyrie, L. & Duplessy, J. C. Changes in North Atlantic deep-water formation associated with the Dansgaard-Oeschger temperature oscillations (60-10 ka). *Quaternary Science Reviews* **21**, 1153–1165 (2002).
57. McManus, J. F., Francois, R., Gherardi, J. M., Keigwin, L. D. & Brown-Leger, S. Collapse and rapid resumption of Atlantic meridional circulation linked to deglacial climate changes. *Nature* **428**, 834–837 (2004).
58. Böhm, E. *et al.* Strong and deep Atlantic meridional overturning circulation during the last glacial cycle. *Nature* 1–17 (2015).
59. Obrochta, S. P., Yokoyama, Y., Morén, J. & Crowley, T. J. Conversion of GISP2-based sediment core age models to the GICC05 extended chronology. *Quaternary Geochronology* **20**, 1–7 (2014).
60. Rignot, E. & Jacobs, S. S. Rapid bottom melting widespread near Antarctic Ice Sheet grounding lines. *Science* **296**, 2020–2023 (2002).

61. Bindschadler, R., Vaughan, D. G. & Vornberger, P. Variability of basal melt beneath the Pine Island Glacier ice shelf, West Antarctica. *Journal of Glaciology* **57**, 581–595 (2011).
62. Straneo, F. & Cenedese, C. The dynamics of Greenland's glacial fjords and their role in climate. *Annual Review of Marine Science* **7**, 89–112 (2015).
63. Holland, P. R., Jenkins, A. & Holland, D. M. The response of ice shelf basal melting to variations in ocean temperature. *Journal of Climate* **21**, 2558–2572 (2008).
64. Sutherland, D. A., Straneo, F. & Pickart, R. S. Characteristics and dynamics of two major Greenland glacial fjords. *Journal of Geophysical Research: Oceans* **119**, 3767–3791 (2014).
65. Jackson, R. H., Straneo, F. & Sutherland, D. A. Externally forced fluctuations in ocean temperature at Greenland glaciers in non-summer months. *Nature Geoscience* **7**, 503–508 (2014).
66. Lambeck, K., Rouby, H., Purcell, A., Sun, Y. & Sambridge, M. Sea level and global ice volumes from the Last Glacial Maximum to the Holocene. *Proceedings of the National Academy of Sciences* **111**, 15296–15303 (2014).